Differential-drag-based roto-translational control for propellant-less spacecraft

Mirko Pastorelli [a], Riccardo Bevilacqua [b,*], Stefano Pastorelli [c]

[a] Department of Mechanical and Aerospace Engineering, Politecnico di Torino, Torino, Italy
[b] Mechanical and Aerospace Engineering Department, University of Florida, MAE-A Building, PO Box 116250, Gainesville, FL 32611-6250, USA
[c] Department of Mechanical and Aerospace Engineering, Room 6939 Politecnico di Torino, Corso Duca degli Abruzzi 24, Torino 10129, Italy

A R T I C L E   I N F O

A B S T R A C T

This paper proposes a novel technique to perform propellant-free chaser–target spacecraft relative maneuvers while simultaneously stabilizing the chaser's attitude with respect to the local vertical local horizontal coordinate system centered at its body center of mass. The control forces required for relative maneuvers at low Earth orbits can be generated by varying the relative aerodynamic drag via maneuverable sails placed in the back-end of the spacecraft. At the same time, aerodynamic torques resulting from the displacement of the centers of pressure of the sails can stabilize the orientation of the spacecraft. In this work, the target vehicle is assumed to maneuver an identical sail in a cooperative fashion and will be centered and attitude-stabilized in its local vertical local horizontal coordinate system. The proposed approach is based on the idea of virtual thrusters, emulating the sail's center of pressure offset in the controller. Several test cases are presented for various existing spacecraft, demonstrating successful propellant-less roto-translational control of the chaser spacecraft.

© 2015 IAA. Published by Elsevier Ltd. All rights reserved.

1. Introduction

Several agencies and universities currently use nano-satellites for a variety of space missions. Some examples include: the CanX-2 Mission: a satellite with a mass of 3.5 kg and about the size of a carton of milk [1]; the *OCSD* mission: a 1.5-unit CubeSat spacecraft with dimensions of approximately 10 by 10 by 16 cm and a mass of approximately 3 kg [2]; the *EDSN*: each satellite is a1.5 unit CubeSat with dimensions of about 10 by 10 by 16 centimeters and a mass of about 2 kg [3]; the *CPOD*: each of the satellites has dimensions of 10 by 10 by 33 cm and a

mass of about 5 kg [4]. Other future missions will be accomplished with the following two satellites: the Atmo-cube, a 1-unit nanosatellite with a mass of 1 kg and dimensions of 10 by 10 by 10 cm [5] and the PADDLES satellite, which is currently under design at the University of Florida and is envisioned to be a 3U CubeSat with a deployable drag sail in the back-end.

In most nanosatellites, the mass and volume available for the propulsion system are very limited. Using differential drag at LEO, mainly for relative maneuvers, represents an alternative to classical propulsion systems.

This technique requires attitude or geometry changes to control the amount of atmospheric drag a satellite encounters in order to change its orbital velocity. This can be accomplished by varying the relative drag area available to the atmosphere between satellites of the same plane, generating the relative control accelerations. Alternatives to modifying

---

Nomenclature

$\vec{a}_{drag}$	= drag acceleration vector [m/s^2]
A	= matrix of the unstable system
A_D	= matrix of the stable system
B	= command matrix
$BCRF$	= body-chaser reference frame
$BTRF$	= body-target reference frame
c_D	= coefficient of drag
$CPOD$	= CubeSat Proximity Operations Demonstration
DCM_T	= rotation matrix between *LTRF* and *EFRF*
DCM_A	= rotation matrix between *LCRF* and *EFRF*
DCM_E	= rotation matrix between *LCRF* and *BCRF*
DCM_C	= rotation matrix between *BCRF* and *EFRF*
DCM	= rotation matrix between *BTRF* and *EFRF*
DCM_{LTRF}^{BTRF}	= rotation matrix between *LTRF* and *BTRF*
DCM_{LCRF}^{LTRF}	= rotation matrix between *LCRF* and *LTRF*
$\overline{e}_{\vartheta}$	= error state vector of attitude control [deg]
$\dot{\overline{e}}_{\vartheta}$	= derivative of error state vector of attitude control [deg/s]
$\overline{e}_{\rho}$	= error state vector of position control [m]
$\dot{\overline{e}}_{\rho}$	= derivative of error state vector of position control [m/s]
$EFRF$	= Earth's fixed reference frame
$EDSN$	= Edison demonstration of SmallSat networks
$f\left(\overline{x}_{LTRF}, \dot{\overline{x}}_{LTRF}\right)$	= nonlinear orbital differential dynamics function
$f(\overline{\delta\vartheta})$	= nonlinear attitude differential dynamics function
$\vec{F}_{DRAG-LCRF}$	= drag force expressed in *LCRF* [N]
$\vec{F}_{DRAG-BCRF}$	= drag force expressed in *BCRF* [N]
$\overline{F}_D$	= drag force [N]
$\overline{\delta\omega}$	= relative angular rate [rad/s]
$\dot{\overline{\delta\omega}}$	= relative angular acceleration [rad/s^2]
$\overline{\delta\vartheta}$	= relative Euler rates of the real system [rad/s]
$\dot{\overline{\delta\vartheta}}_d$	= relative Euler rates of the linearized system [rad/s]
$\dot{\overline{\delta\vartheta}}$	= relative Euler acceleration of the real system [rad/s^2]
$\ddot{\overline{\delta\vartheta}}_d$	= relative Euler acceleration of the linearized system [rad/s^2]
$\vec{r}_{rel}$	= relative position of the *BCRF* in *LTRF* of the real system [m]
$\dot{\vec{r}}_{rel}$	= relative velocity of the *BCRF* in *LTRF* of the real system [m/s]
$\ddot{\vec{r}}_{rel}$	= relative acceleration of the *BCRF* in *LTRF* of the real system [m/s^2]
$\overline{x}_D$	= relative state position vector of the linearized system
$\dot{\overline{x}}_D$	= derivative of the relative state position vector of the linearized system
$\overline{x}$	= relative state position vector of the real system
$\dot{\overline{x}}$	= derivative of the relative state position vector of the real system
H	= map matrix of virtual thrusters' distribution
$\overline{K}_2$	= gain matrix of attitude linear model
$\overline{K}_1$	= gain matrix of attitude linear model
J	= inertia tensor [kg m^2]
L	= rotation matrix of position model
$LCRF$	= *LVLH*-chaser reference frame
LEO	= low Earth orbit
$LVLH$	= local vertical local horizontal
$LTRF$	= *LVLH*-target reference frame
LQR	= linear quadratic regulator
m_{chaser}	= mass of the spacecraft [kg]
$\overline{M}_{xz}$	= torque vector [N m]
$OCSD$	= optical communications and sensor demonstration
P	= gain matrix of the Lyapunov function
$PADDLES$	= propellant-less atmospheric differential drag LEO satellite
Q_{LQR}	= weight matrix of the LQR (state vector weight)
R_{LQR}	= weight matrix of the LQR (control vector weight)
S	= total area of the spacecraft [m^2]
S_{Sail}	= sail surface area [m^2]
S_{min}	= satellite surface area [m^2]
ρ	= air density [kg/m^3]
UFL	= University of Florida
$\overline{u}$	= signal command virtual thrusters and position control
$\hat{u}$	= command virtual thrusters
$\overline{u}_D$	= desired position control command
$\overline{u}_{\vartheta}$	= desired attitude control command
u_{DRAG}	= modulus of drag acceleration [m/s^2]
$\vec{v}_{sat}$	= velocity of the spacecraft [m/s]
$\vec{v}_{rel}$	= relative velocity between the spacecraft and the rotating atmosphere [m/s]
$\vec{v}_{atm}$	= velocity of the rotating atmosphere [m/s]
v	= variable of command
V	= Lyapunov function
$\dot{V}$	= derivative of the Lyapunov function
$\overline{w}$	= nonlinear attitude function
$X\left(\overline{\vartheta}\right)$	= kinematics matrix relating angular velocity and Euler angles
X_{gg}	= *X*-coordinate of the center of pressure [m]
X_g	= vector of the virtual thrusters *X*-coordinates [m]
Z_{gg}	= *Z*-coordinate of the center of pressure [m]
Z_g	= vector of the virtual thrusters *Z*-coordinates [m]

area profiles include reorientation of solar panels or deployment of a specifically designed drag sail (see Fig. 1).

Several works have investigated the differential drag method to show its feasibility. An optimal control approach to the problem of the differential drag-based positional control for the rendezvous maneuver was proposed by Lamberto Dell'Elce and Gaëtan Kerschen [6]. Shuford [7] showed that a mechanism of separation and formation of a CubeSat constellation based on the differential drag is possible by varying cross-sectional areas through rotation
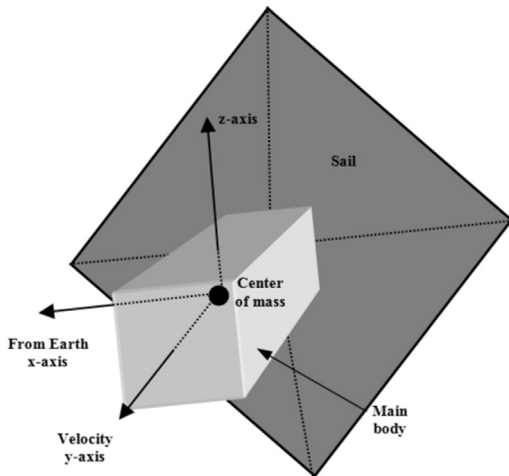
Fig. 1. 3-Unit CubeSat with the drag sail. This concept represents the PADDLES spacecraft developed at the University of Florida. The axes shown represent the LHLV reference frame centered at the center of mass of the spacecraft. The PADDLES will be required to fly ram-aligned, i.e. with the sail normal to the y axis.

of the spacecraft. Kumar et al. [8] investigated the feasibility of using differential drag as a means of nano-satellite formation control and showed that they could maintain the formation separation with reasonable accuracy. Palmerini [9] investigated the role of differential drag as an advantageous propulsion-free strategy to achieve desired orbital configurations of satellite clusters. In this paper, the differential drag was obtained by re-orientation of the spacecraft combined with deployment/retraction of a control surface. Bevilacqua and Romano [10] proposed a new two-phase control logic for the relative orbit stabilization and the subsequent rendezvous of multiple spacecraft by exploiting differential atmospheric drag. Each spacecraft was assumed to include a rotating drag plate capable of varying the atmospheric drag. The maneuver is conducted in two successive phases: (1) stabilization phase: each chaser spacecraft is driven to an equilibrium periodic orbit around the target, and (2) rendezvous phase: each chaser spacecraft converges to the target. Pérez and Bevilacqua [11] developed a differential drag-based full state feedback control for spacecraft rendezvous maneuvers with three possible commands to ensure the time derivative of the selected Lyapunov function is negative semi-definite. The same authors [12] further developed the Lyapunov-based control technique into an adaptive control strategy. This strategy provided to adapt the Lyapunov function at each time-step, in relationship to the magnitude of the evaluated drag acceleration. The adaptive strategy takes into account the effects of the variable atmospheric density and any non-linearities.

The literature discussed used differential drag to control only the relative position between two satellites in the orbital plane, while leaving magnetic instruments and reaction wheels with the task of attitude control. In many works, attitude stabilization is not even considered and the maneuvers are executed only when satellite and atmosphere have a favorable relative orientation, i.e., when the drag force is

sufficient. This occurs when the upcoming wind is perpendicular (or very close to) to the designated drag surface.

Attitude control using atmospheric-based actuation, while maintaining position control, is the natural evolution of this research. In this work, the differential drag concept is expanded and for the first time in literature, it is proven to be an effective means of attitude stabilization. The most important starting point for the development of the method here proposed was given by Curti et al. [13]. Their work presented a Lyapunov-based thruster on/off activation strategy to control the spacecraft roto-translational motion. This approach resulted in spacecraft tracking of the desired linear reference models in both position and orientation.

The concepts of Ref. [13] led to the idea of virtual thrusters this paper introduces. A spacecraft equipped with a drag sail (Fig. 1) can be conceptualized as a vehicle with virtual thrusters mounted in the back-end. These thrusters are activated using a strategy similar to the one in Ref. [13] to perform roto-translational motion control.

By asymmetrically activating the thrusters, control torques are generated. These commands are then translated into displacements for the drag sail center of pressure. In addition these commands dictate when to open or close the sail. In particular, the barycenter of the active virtual thrusters is computed. This point is used as the desired location for the center of pressure of the drag sail. In addition, it is assumed that the net force from the active thrusters is equivalent to the drag force. By using this emulation strategy, a Lyapunov-based controller with on/off actuators can be used, simultaneously controlling both positional and rotational motion.

The deployment/retraction of the sail, as well as its center of pressure offset motion, may have an effect on the spacecraft dynamics. Due to conservation of linear and angular momentum, the spacecraft dynamics is dependent on the types of mechanisms utilized. In this work it is assumed that the sail mechanical system is much lighter than the spacecraft and such effects are neglected. In addition, this work does not focus on the potential mechanical solutions to obtain sail deployment and retraction, nor does it propose a practical solution to the physical implementation of displacing the center of pressure.

The contribution to the state of the art of this research consists mainly in the idea of utilizing drag to control both the relative motion and orientation of the satellite. To the authors' knowledge this is the first proposal of using this combined approach. In addition, the virtual thruster strategy is a clever way to utilize already present drag aerodynamic torques, while enabling Lyapunov-based on-off control of the drag sail and its center of pressure location. In order to demonstrate the feasibility of the proposed approach, the following spacecraft are imagined to have a drag sail in order to execute propellant-less rendezvous and rephasing: CanX-2, OCSD, EDSN, CPOD, and Atmocube. In addition, the PADDLES satellite is used to analyze the spacecraft characteristics' effects on the control performances.

This paper is organized as follows: first, it introduces the concept of virtual thrusters and the idea of the displacement of the center of pressure by calculation of the barycenter. The following section is about the atmospheric drag and its

mathematical expression. Following, is a section on space vehicle mechanics, illustrating all the reference frames and the analytical expressions of roto-translational dynamics. The virtual thrusters' distribution and the idea of the map matrix as a mean of attitude control follows. The next section introduces the control command strategy based on the linear reference models and the Lyapunov-based approach. Finally, a numerical simulations section is presented for a set of real satellites that are imagined to be maneuvered with a sail placed in their back-end. This section also investigates the behavior of two satellites which have to reach the rendezvous condition with different characteristics (gains, surface area of the sail). The last section discusses the conclusions of this work.

2. The concept of differential drag-based attitude and position control

This section introduces the concept for LEO propellant-less spacecraft planar maneuvers using atmospheric differential drag, for both in-plane position (i.e. X and Y in the *LVLH* frame) and ram attitude (i.e. z and x-body axes) (Fig. 2).
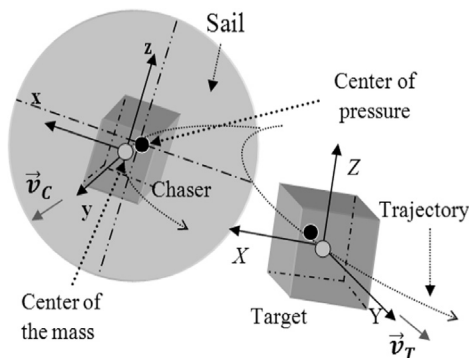

Fig. 2. Chaser, target, and the drag sail concept.

The proposed approach is based on imagining 8 virtual thrusters (Fig. 3) generating an overall force only along the negative y body axis of the chaser such that the overall magnitude equals the actual drag force. The thrusters are activated with the goal of performing position control, while maintaining a satisfactory alignment of the chaser's y body axis with its velocity vector, in order to maximize the sail's drag. A non-symmetric activation of the virtual thrusters implies a displacement of the sail's center of pressure with respect to its geometric center, thus generating a control torque. The command position for the sail's center of pressure is computed as the barycenter of the active virtual thrusters. For example, only one active thruster implies the center of pressure to be located at the thruster's position, two thrusters imply the center of pressure to be located at the mid-point along the line described by the thrusters' locations, and so on.

The target vehicle is assumed to maneuver an identical sail in a cooperative fashion, while centered and attitude-stabilized in its *LVLH* reference frame.

In order to preserve the chaser's attitude, the control law is divided into two logical loops; one for the position and one for the attitude. The attitude loop stabilizes the chaser's orientation continuously when its sail is opened through impulsive movements of the sail's center of pressure. The position loop tracks the desired maneuver. The attitude loop has higher priority (i.e., it can force opening of the sail regardless of the other states) if the attitude error exceeds the chosen tolerance.

The above enables attitude stabilization, resulting in the correct orientation of the sail with respect to the velocity vector. In order to simulate the behavior of a potential real drag sail mechanical system, both the opening/closing of the sail and its displacement of the center of pressure from the center of mass are simulated with realistic dynamic response. In particular, the simulated time responses are obtained as the responses from first order dynamical systems excited by step functions.

The factors affecting the behavior of the system include the following: atmospheric density, orientation of the spacecraft,
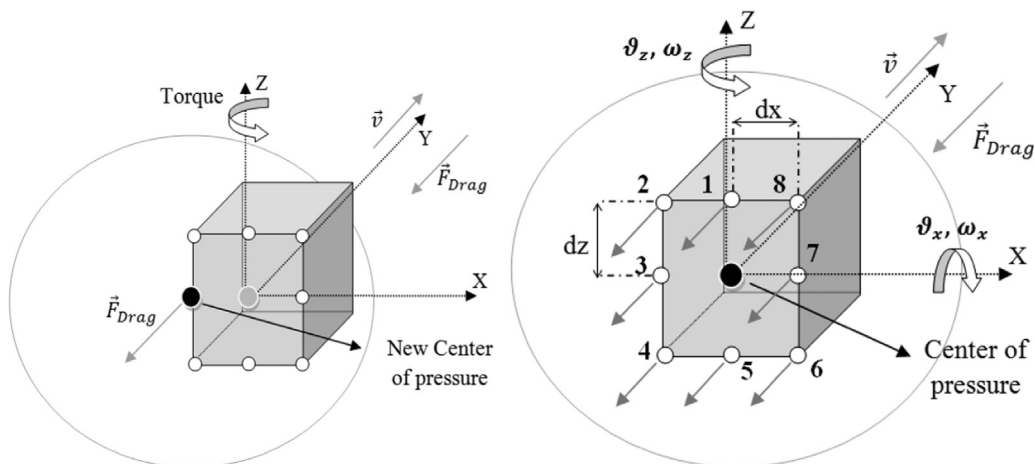

Fig. 3. Displacement of center of pressure (LEFT): in this example the sail (circle in the image) is shifted to the left with respect to the geometric center of the spacecraft. Virtual Thrusters Concept (RIGHT): in this example, the 8 thrusters are all active, resulting in the sail being centered with respect to the spacecraft.

orbital characteristics, dynamics of the mechanical system, chosen Lyapunov function, characteristics of the spacecraft system, and relative initial conditions. The simulations section discusses the limits of the proposed concept.

3. Atmospheric drag in LEO

The acceleration due to drag on a satellite is given by:

$$\vec{a}_{drag} = -\frac{1}{2}\rho\frac{c_D S}{m}v_{rel}^2\frac{\vec{v}_{rel}}{|\vec{v}_{rel}|} \tag{1}$$

where c_D indicates the coefficient of drag, dependent on the spacecraft material and its aerodynamic shape [14], m is the satellite's mass, S is the cross-sectional area orthogonal to the velocity direction, and ρ is the atmospheric density. $\vec{v}_{rel}$ is the velocity of the satellite relative to the atmosphere.

For identical satellites flying in the same formation and in the same plane, all of these parameters will be approximately equal, except for the atmospheric density, and drag surface, if not oriented the same way. It is primarily the density fluctuations in the Earth's atmosphere that cause acceleration differences between satellites flying in formation.

The density of the upper atmosphere is subjected to variations caused by three main factors: (1) heterogeneous molecules, (2) radiation from the Sun, and (3) Earth's geomagnetic activity.

The relative velocity $\vec{v}_{rel}$, the velocity relative to the atmosphere, depends on the accuracy of the a-priori estimate and the results of any orbit determination processes. Because it is generally a large squared quantity, it becomes a very important factor in the calculation of the acceleration. However, it has received surprisingly little analysis in the literature. A common assumption [14] is that the lower atmosphere rotates with the Earth, so that a vector summation for the velocity values can be performed. The upper atmosphere winds can be several hundreds m/s which can have a large effect on the drag acceleration. However, they are particularly unknown, unmodeled, and unpredicted.

$$\vec{v}_{rel} = \vec{v}_{sat} + \vec{v}_{atm} \tag{2}$$

The satellite surface can be simple (spherical shape or constant area orthogonal to the velocity vector), or complex (all others). The simple case is not very common within the context of the entire satellite catalog, but it provides opportunities to investigate the variability of the other parameters. The cross sectional area changes constantly (unless there is precise attitude control or the satellite is a sphere). This variable can change by a factor of 10 or more depending on the specific satellite configuration [14]. Global atmospheric models are often used for modeling solar pressure accelerations, but seldom if ever, for atmospheric drag. The most scientifically accurate approach is to input the attitude (quaternions, direction cosines, etc.) into the orbit determination solution and simply account for the actual or predicted attitude, which gives the frontal area exposed in the relative velocity direction. However, very few programs are able to accomplish this.

Given the above discussion, it is common to use a combined parameter which incorporates mass, area, and coefficient of drag, called the ballistic coefficient (BC), which is defined as

$$BC = c_D S/m \tag{3}$$

The ballistic coefficient will vary, sometimes by a large factor.

Among the examined parameters, assuming the mass of the spacecraft and the drag coefficient are fixed, the only variable parameter is S. Modifications of the cross sectional area of the sail are then assumed to be the only drivers for the differential drag.

4. Space vehicle mechanics

The coordinate systems in Fig. 4 are used for the derivation of the roto-translational mechanics equations for space vehicle relative motion [15].

4.1. Translational mechanics

The equations for the translational motion of each spacecraft are as follows:

$$\ddot{\vec{r}} + \mu\frac{\vec{r}}{r^3} = \vec{f} \tag{4}$$

where $\vec{f}$ is the net drag acceleration and the perturbing forces per unit mass and μ is the gravitational parameter. The relative position between chaser and target is given in *LTRF* by the following differential equation, already assumed to be confined to the orbital plane:

$$\ddot{\bar{r}}_{rel} = f\left(\bar{r}_{rel}, \dot{\bar{r}}_{rel}\right) + \frac{1}{m}\bar{F}_{DRAG-LTRF} \tag{5}$$

where: $\bar{F}_{DRAG-LTRF}$ is the drag force acting on the chaser expressed in *LTRF* and $f\left(\bar{r}_{rel}, \dot{\bar{r}}_{rel}\right)$ is the non linear function including the perturbing differential forces. It is assumed that the drag force in *LCRF* is always directed opposite to the velocity vector so that the force has only one non-zero
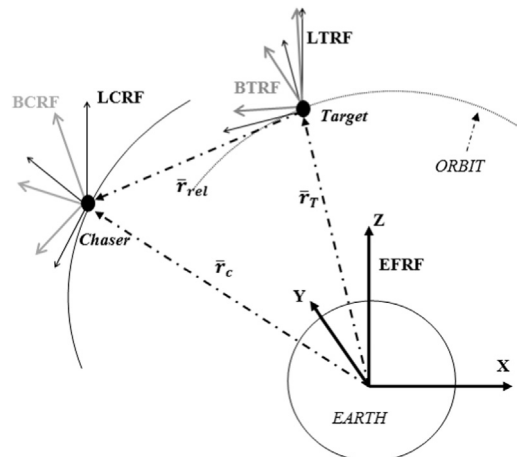

Fig. 4. Reference frames: *BCRF, BTRF, LCRF, LTRF, EFRF.*

element, i.e.:

$$\overline{F}_{DRAG-LCRF} = m \cdot \begin{bmatrix} 0 \\ -1 \\ 0 \end{bmatrix} u_{DRAG} \tag{6}$$

where u_{DRAG} is the norm of the drag acceleration so that

$$\overline{F}_{DRAG-LTRF} = DCM_{LCRF}^{LTRF} \cdot \overline{F}_{DRAG-LCRF} = DCM_T \cdot (DCM_A)^T \cdot \overline{F}_{DRAG-LCRF} \tag{7}$$

The in-plane state vector of relative position and velocity between chaser and target is defined as

$$\overline{x} = [x, y, \dot{x}, \dot{y}]$$

Thus, Eq. (5) becomes

$$\dot{\overline{x}} = f\left(\overline{x}, \dot{\overline{x}}\right) + LB\vec{a}_{drag} \tag{8}$$

$$\dot{\overline{x}} = \begin{bmatrix} \dot{x} \\ \dot{y} \\ \ddot{x} \\ \ddot{y} \end{bmatrix} = \begin{bmatrix} \dot{x} \\ \dot{y} \\ f\left(\overline{r}_{rel}, \dot{\overline{r}}_{rel}\right) \end{bmatrix} + \begin{bmatrix} 0 & 0 & 0 & 0 \\ 0 & 0 & 0 & 0 \\ 0 & 0 & & \\ 0 & 0 & DCM_{LCRF}^{LTRF} \end{bmatrix} \begin{bmatrix} 0 \\ 0 \\ 0 \\ 1 \end{bmatrix} \overline{\overline{u}} \cdot u_{DRAG} \tag{9}$$

and

$$L = \begin{bmatrix} 0 & 0 & 0 & 0 \\ 0 & 0 & 0 & 0 \\ 0 & 0 & & \\ 0 & 0 & DCM_{LCRF}^{LTRF} \end{bmatrix} \quad B = \begin{bmatrix} 0 \\ 0 \\ 0 \\ 1 \end{bmatrix} \quad \overline{\overline{u}} = \begin{Bmatrix} 1 \\ 0 \end{Bmatrix} \tag{10}$$

where $\overline{\overline{u}} = 1$ when the sail of the spacecraft is open and $\overline{\overline{u}} = 0$ when the sail is closed.

4.2. Rotational mechanics

The spacecraft attitude dynamics is represented by [16]

$$\overline{M} = J\dot{\overline{\omega}} + (\overline{\delta\omega} + \overline{\omega}_{LVLH}) \times J(\overline{\delta\omega} + \overline{\omega}_{LVLH}) \tag{11}$$

That can be expressed as

$$\overline{\delta\omega}^{\cdot} = J^{-1}\overline{M} - J^{-1}[(\overline{\delta\omega} + \overline{\omega}_{LVLH}) \times J(\overline{\delta\omega} + \overline{\omega}_{LVLH})] \tag{12}$$

where J is the inertia matrix of the chaser, $\overline{\delta\omega} = \overline{\omega} - \overline{\omega}_{LVLH}$ is the relative angular velocity of the chaser with respect to the LCRF, expressed in the chaser frame, whose respective angular velocities are $\overline{\omega}$ and $\overline{\omega}_{LVLH}$, and M is the torque acting on the chaser. It is also assumed that $\overline{\omega}_{LVLH}$ is a constant vector in the inertial reference frame (i.e., the orbit is circular or with very small residual eccentricity), while natural drifts of the orbital plane are neglected. The kinematics equation in terms of relative Euler Angles (between BCRF and LCRF) is

$$\overline{\delta\omega} = X(\overline{\delta\vartheta}) \cdot \overline{\delta\vartheta}^{\cdot} \tag{13}$$

Substituting Eq. (13) into Eq. (12), leads to

$$d\left(\frac{X(\overline{\delta\vartheta}) \cdot \overline{\delta\vartheta}^{\cdot})}{dt = J^{-1}\overline{M} - J^{-1}\left[(X(\overline{\delta\vartheta}) \cdot \overline{\delta\vartheta}^{\cdot} + \overline{\omega}_{LVLH}) \times J(X(\overline{\delta\vartheta}) \cdot \overline{\delta\vartheta}^{\cdot} + \overline{\omega}_{LVLH})\right]}\right) \tag{14}$$

That becomes:

$$X(\overline{\delta\vartheta}) \cdot \overline{\delta\vartheta}^{\cdot\cdot} + X\left(\overline{\delta\vartheta}^{\cdot}\right) \cdot \overline{\delta\vartheta}^{\cdot} = J^{-1}\overline{M} - J^{-1}[(X(\overline{\delta\vartheta}) \cdot \overline{\delta\vartheta}^{\cdot}$$

$$+ \overline{\omega}_{LVLH}) \times J(X(\overline{\delta\vartheta}) \cdot \overline{\delta\vartheta}^{\cdot} + \overline{\omega}_{LVLH})]\overline{\delta\vartheta}^{\cdot\cdot} = X\left(\overline{\delta\vartheta}\right)^{-1} \cdot J^{-1}\overline{M}$$

$$- X\left(\overline{\delta\vartheta}\right)^{-1} \cdot J^{-1}[(X(\overline{\delta\vartheta}) \cdot \overline{\delta\vartheta}^{\cdot} + \overline{\omega}_{LVLH}) \times J(X(\overline{\delta\vartheta}) \cdot \overline{\delta\vartheta}^{\cdot}$$

$$+ \overline{\omega}_{LVLH})] - X\left(\overline{\delta\vartheta}\right)^{-1} \left(X\left(\overline{\delta\vartheta}^{\cdot}\right)\right) \cdot \overline{\delta\vartheta}^{\cdot} \tag{15}$$

Eq. (15) can be compacted in the form:

$$\overline{\delta\vartheta}^{\cdot\cdot} = X\left(\overline{\delta\vartheta}\right)^{-1} \cdot J^{-1}\overline{M} + f(\overline{\delta\vartheta}^{\cdot}, \overline{\delta\vartheta}) \tag{16}$$

Since torques only around the x-axis and z-axis of the body frame can be generated, Eq. (16) can be written as

$$\overline{\delta\vartheta}^{\cdot\cdot}_{xz} = G\left(\overline{\delta\vartheta}\right)_{xz} \cdot \overline{M}_{xz} + f(\overline{\delta\vartheta}^{\cdot}_{xz}, \overline{\delta\vartheta}_{xz}) \tag{17}$$

where

$$G\left(\overline{\delta\vartheta}\right)_{xz} = X\left(\overline{\delta\vartheta}\right)^{-1} \cdot J^{-1}\Big|_{xz}$$

In the previous equations, the subscript xz indicates reduced vectors (only the x and z components are retained) and reduced matrices (only the rows and columns corresponding to x and z are retained). The Euler's angles errors between BCRF and LCRF are obtained considering the direction cosine matrices DCM_A and DCM_C. The direction cosine matrix of the Euler's angles error is found as follows:

$$DCM_E = DCM_B \cdot DCM_A^T \tag{18}$$

From DCM_E the Euler angles between BCRF and LCRF can be extracted, using the rotation sequence XYZ. For example, the direction of the drag force acting on the chaser can be found as

$$\vec{F}_{DRAG-BCRF} = DCM_E \cdot \vec{F}_{DRAG-LCRF} \tag{19}$$

5. Virtual thrusters distribution matrix structure

In this work, an 8 virtual thrusters distribution is considered and the required torque M is produced by the combined firing of the virtual thrusters (see Fig. 3). The virtual thrusters can generate an overall force only along the negative y direction such that the total magnitude equals the net drag force. Let $\hat{u} = u_a \cdot [u_1, u_2, ..., u_8]^T = u_a \cdot \overline{u}$ be the vector of the thrusters, where:

$$\overline{u}_i = \begin{cases} 0 & i\text{th thruster off} \\ 1 & i\text{th thruster on} \end{cases} \quad i = 1, 2..., 8 \tag{20}$$

with: u_a being the positive value of the available thrust of the thrusters. It is important to stress that u_a is a virtual magnitude, so it acts as placeholder and is assigned the appropriate value at each time step, such that $\|\hat{u}\| = F_{DRAG}$ at all times. The vector $\overline{u} = [u_1, u_2, ..., u_8]^T$ is the binary vector called the active thrusters' configuration at the time t. This vector will be allowed to have negative components later on, when discussing the spacecraft relative motion control, to represent a second vehicle's activation of the virtual thrusters.

Let the augmented torque vector be

$$\overline{M} = H\overline{u} \cdot u_a \tag{21}$$

where H is the 4×8 thrusters' distribution matrix related

to the geometrical structure of the virtual thrusters placement on the spacecraft. The vector in Eq. (21) has a *0* first component added to the classical 3-component torque vector, for convenience of use in the following derivations.

To define $\overline{H}$ the scheme of Figs. 3 and 5 is considered.

dx and dz are the moment arms of the thrusters with respect to the center of the mass. The thrusters are numbered from 1 to 8.

The $\overline{H}$ matrix is defined as

$$\overline{H} = \begin{bmatrix} 0 & 0 & 0 & 0 & 0 & 0 & 0 & 0 \\ 0 & 0 & 0 & 0 & 0 & 0 & 0 & 0 \\ dz & dz & 0 & -dz & -dz & -dz & 0 & dz \\ 0 & dx & dx & dx & 0 & -dx & -dx & -dx \end{bmatrix} \quad (22)$$

A reference frame centered in the center of the mass of the spacecraft can be defined, assuming homogeneous mass distribution for simplicity, so that the coordinates of each virtual thruster in the body frame can be written as

N	1	2	3	4	5	6	7	8	
X	0	$-dx$	$-dx$	$-dx$	0	$-dx$	dx	dx	(23)
Z	dz	dz	0	$-dz$	$-dz$	$-dz$	0	dz	

6. Lyapunov-based control command strategies based on linear reference models

This section introduces the command strategy based on the tracking of the dynamics of a reference linear model. There are two different approaches for position and attitude control which result in similar control laws and are outlined in the following section.

6.1. Tracking error equation for position

A linearized model which represents the relative motion of spacecraft under the influence of the J_2 perturbation was developed by Schweighart and Sedwick (Ref. [17]). Adding the control acceleration vector $\overline{u}_D$, where *D* stands for desired, to the Schweighart and Sedwick
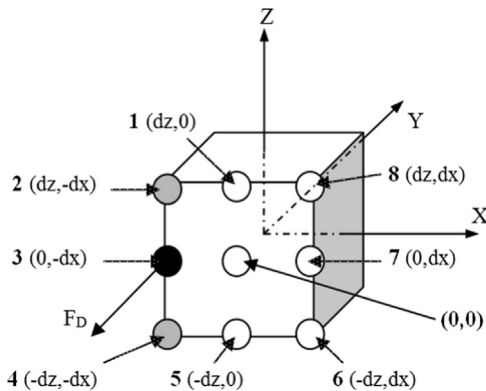
Fig. 5. Selection of the center of pressure. In this example thrusters 2 and 4 are active, which are highlighted in grey color. The resulting center of pressure is the black circle, which in this case overlaps with the location of thruster 3. The axes form a coordinate system in the body reference frame.

equations, the following system of linear equations in the *LTRF* is obtained.

$$\dot{\overline{x}}_D = A\overline{x}_D + B\overline{u}_D \quad (24)$$

where *A* and *B* are the following matrices and $\overline{x}_D$ is the relative position state vector:

$$A = \begin{vmatrix} 0_{2\times2} & I_{2\times2} \\ b & 0 & 0 & a \\ 0 & 0 & -a & 0 \end{vmatrix} \quad B = \begin{bmatrix} 0 \\ 0 \\ 0 \\ 1 \end{bmatrix} \quad \overline{x}_D = \begin{bmatrix} x_D \\ y_D \\ \dot{x}_D \\ \dot{y}_D \end{bmatrix} \quad (25)$$

$a = 2cn$ and $b = (5c^2 - 2)n^2$

$$c = \sqrt{1 + \frac{3J_2 R}{8r_T^2}[1 + 3\,\cos(2i_{ref})]}$$

where *n* is the mean motion of the target, J_2 is the second zonal harmonic, *R* is the Earth mean radius, r_T is the target's orbit radius, and i_{ref} is the target's inclination. It is important to note that the control action is only along the *y* direction.

Since the dynamics of Eq. (25) is unstable, a Linear Quadratic Regulator (LQR) feedback controller is used obtaining a stable linear model for the Lyapunov control strategy.

$$\overline{u}_D = -K\overline{x}_D \quad A_D = A - BK \quad \dot{\overline{x}}_D = A_D\overline{x}_D \quad (26)$$

where *K* is the control gain matrix found by solving the LQR problem, thus ensuring A_D to be Hurwitz and $\overline{x}_D$ is the solution of the linear model.

Defining the error variable $\overline{e}_\rho = \overline{x} - \overline{x}_D$ between Eq. (8) and the evolution of Eq. (26), leads to

$$\dot{\overline{x}} - \dot{\overline{x}}_D = f(\overline{x}, \dot{\overline{x}}) + LB\overline{u} \cdot u_{DRAG} - A_D\overline{x}_D$$

$$\dot{\overline{e}}_\rho = f(\overline{x}, \dot{\overline{x}}) + LB\overline{u} \cdot u_{DRAG} + A_D\overline{x} - A_D\overline{x} - A_D\overline{x}_D$$

$$\dot{\overline{e}}_\rho = A_D\overline{e}_\rho + f(\overline{x}, \dot{\overline{x}}) + LB\overline{u} \cdot u_{DRAG} - A_D\overline{x} \quad (27)$$

6.2. Attitude reference model tracking error equation

Let $\overline{\delta\vartheta}_d$ be the solution of the following equation [13]:

$$\overline{\delta\vartheta}^{\,\cdot\cdot}{}_d + \overline{K}_1\overline{\delta\vartheta}^{\,\cdot}{}_d + \overline{K}_2\overline{\delta\vartheta}_d = \overline{u}_\vartheta \quad (28)$$

where $\overline{K}_1$ and $\overline{K}_2$ are two 2-by-2 positive definite matrices. $\overline{\delta\vartheta}_d$ represents the desired relative orientation of the *BCRF* with respect to the *LCRF*.

The input vector $\overline{u}_\vartheta$ is the variable of command (a virtual torque).

Subtracting the linear system, Eq. (28), from the non-linear system of Eq. (17) leads to

$$\overline{\delta\vartheta}^{\,\cdot\cdot}{}_{xz} - \overline{\delta\vartheta}^{\,\cdot\cdot}{}_d = f(\overline{\delta\vartheta}^{\,\cdot}{}_{xz}) + \overline{K}_1\overline{\delta\vartheta}^{\,\cdot}{}_d + \overline{K}_2\overline{\delta\vartheta}_d - \overline{u}_\vartheta + G(\vartheta)_{xz} \cdot \overline{M}_{xz} \quad (29)$$

And defining $\overline{e}_{\vartheta xz} = \overline{\delta\vartheta}_{xz} - \overline{\delta\vartheta}_d$

$$\overline{e}^{\,\cdot\cdot}{}_{\vartheta xz} = f(\overline{\delta\vartheta}^{\,\cdot}{}_{xz}) + \overline{K}_1\overline{\delta\vartheta}^{\,\cdot}{}_d + \overline{K}_2\overline{\delta\vartheta}_d + \overline{K}_1\overline{\delta\vartheta}^{\,\cdot}{}_{xz} + \overline{K}_2\overline{\delta\vartheta}_{xz}$$
$$- \overline{K}_1\overline{\delta\vartheta}^{\,\cdot}{}_{xz} - \overline{K}_2\overline{\delta\vartheta}_{xz} - \overline{u}_\vartheta + G(\vartheta)_{xz} \cdot \overline{M}_{xz}$$

$$\overline{e}\cdot\cdot_{\vartheta xz}+\overline{K}_1\overline{\delta\vartheta}\,\dot{}_{xz}+\overline{K}_2\overline{\delta\vartheta}_{xz}-\overline{K}_1\overline{\delta\vartheta}\,\dot{}_d-\overline{K}_2\overline{\delta\vartheta}_d$$
$$=f\left(\overline{\delta\vartheta}\,\dot{}_{xz}\right)+\overline{K}_1\overline{\delta\vartheta}\,\dot{}_{xz}+\overline{K}_2\overline{\delta\vartheta}_{xz}-\overline{u}_2+G(\vartheta)_{xz}\cdot\overline{M}_{xz}$$

$$\overline{e}\cdot\cdot_{\vartheta xz}+\overline{K}_1\dot{\overline{e}}_{\vartheta xz}+\overline{K}_2\overline{e}_{\vartheta xz}=f\left(\overline{\delta\vartheta}\,\dot{}_{xz}\right)+\overline{K}_1\overline{\delta\vartheta}\,\dot{}_{xz}+\overline{K}_2\overline{\delta\vartheta}_{xz}$$
$$-\overline{u}_\vartheta+G(\vartheta)_{xz}\cdot\overline{M}_{xz} \qquad (30)$$

And, introducing

$$\overline{v}_\vartheta=f\left(\overline{\delta\vartheta}\,\dot{}_{xz}\right)+\overline{K}_1\overline{\delta\vartheta}\,\dot{}_{xz}+\overline{K}_2\overline{\delta\vartheta}_{xz} \qquad (31)$$

leads to

$$\overline{e}\cdot\cdot_{\vartheta xz}+\overline{K}_1\dot{\overline{e}}_{\vartheta xz}+\overline{K}_2\overline{e}_{\vartheta xz}=\overline{v}_\vartheta-\overline{u}_\vartheta+G(\vartheta)_{xz}\cdot\overline{M}_{xz} \qquad (32)$$

Defining the error-state vectors:

$$\overline{e}_\vartheta=\begin{bmatrix}\overline{e}_{\vartheta x} & \overline{e}_{\vartheta z} & \dot{\overline{e}}_{\vartheta x} & \dot{\overline{e}}_{\vartheta z}\end{bmatrix}$$
$$\dot{\overline{e}}_\vartheta=\begin{bmatrix}\dot{\overline{e}}_{\vartheta x} & \dot{\overline{e}}_{\vartheta z} & \ddot{\overline{e}}_{\vartheta x} & \ddot{\overline{e}}_{\vartheta z}\end{bmatrix} \qquad (33)$$

and in matrix form:

$$\begin{bmatrix}\dot{\overline{e}}_\vartheta\end{bmatrix}=\begin{bmatrix}0_{2\times2} & I_{2\times2} \\ -\overline{K}_2 & -\overline{K}_1\end{bmatrix}\begin{bmatrix}\overline{e}_\vartheta\end{bmatrix}+\begin{bmatrix}0_{2\times2} & 0_{2\times2} \\ 0_{2\times2} & G(\vartheta)_{xz}\end{bmatrix}\begin{bmatrix}0 \\ 0 \\ \overline{M}_{xz}-G(\vartheta)_{xz}^{-1}(\overline{v}_\vartheta-\overline{u}_\vartheta)\end{bmatrix} \qquad (34)$$

Considering the $\overline{H}$ matrix, $\overline{M}_{xz}$ can be expressed as

$$\begin{bmatrix}0 \\ 0 \\ \overline{M}_{xz}\end{bmatrix}=\overline{H}\overline{u}\cdot u_a \qquad (35)$$

And defining:

$$\overline{w}=\begin{bmatrix}0 \\ 0 \\ G(\vartheta)_{xz}^{-1}(\overline{v}_\vartheta-\overline{u}_\vartheta)\end{bmatrix} \qquad (36)$$

So that

$$\begin{bmatrix}\dot{\overline{e}}_\vartheta\end{bmatrix}=\begin{bmatrix}0_{2\times2} & I_{2\times2} \\ -\overline{K}_2 & -\overline{K}_1\end{bmatrix}\begin{bmatrix}\overline{e}_\vartheta\end{bmatrix}+\begin{bmatrix}0_{2\times2} & 0_{2\times2} \\ 0_{2\times2} & J_{xz}^{-1}\end{bmatrix}[\overline{H}\overline{u}\cdot u_a-\overline{w}] \qquad (37)$$

$$\begin{bmatrix}\dot{\overline{e}}_\vartheta\end{bmatrix}=[A]\begin{bmatrix}\overline{e}_\vartheta\end{bmatrix}+[B][\overline{H}\overline{u}\cdot u_a-\overline{w}] \qquad (38)$$

6.3. Lyapunov position control strategy

The following Lyapunov function is selected

$$V=e^TPe \qquad (39)$$

With $P=P^T>0$. Differentiating Eq. (39) along the trajectories in Eq. (27) leads to

$$\dot{V}=\dot{\overline{e}}_\rho P\overline{e}_\rho+\overline{e}_\rho^TP\dot{\overline{e}}_\rho \qquad (40)$$

$$\dot{V}=\overline{e}_\rho^TPA\overline{e}_\rho+\overline{e}_\rho^TA^TP\overline{e}_\rho+2\overline{e}_\rho^TP\left(f\left(\overline{x},\dot{\overline{x}}\right)+LB\overline{u}\cdot u_{DRAG}-A_D\overline{x}\right) \qquad (41)$$

For a symmetric positive definite matrix Q, the matrix P is found as unique solution of the Lyapunov Equation.

$$PA+A^TP=-Q \qquad (42)$$

Substituting Eq. (42) into Eq. (41) leads to

$$\dot{V}=-\overline{e}_\rho^TQ\overline{e}_\rho+2\overline{e}_\rho^TP\left(f\left(\overline{x},\dot{\overline{x}}\right)+LB\overline{u}\cdot u_{DRAG}-A_D\overline{x}\right) \qquad (43)$$

Which is rearranged into

$$\dot{V}=-\overline{e}_\rho^TQ\overline{e}_\rho+2\overline{e}_\rho^TP\left(f'\left(\overline{x},\dot{\overline{x}}\right)+LB\overline{u}\cdot u_{DRAG}\right) \qquad (44)$$

with f including the term $-A_D\overline{x}$. Since the first term is always negative definite, in order to be able to prove stability via Lyapunov analysis, the controller needs to be derived to ensure the second terms is at least negative semi-definite.

$$2\overline{e}_\rho^TP\left(f'\left(\overline{x},\dot{\overline{x}}\right)+LB\overline{u}\cdot u_{DRAG}\right)<0 \qquad (45)$$

The term $f'\left(\overline{x},\dot{\overline{x}}\right)$ cannot be influenced by the control variable, thus the control strategy is chosen as

$$2\overline{e}_\rho^TPLB\overline{u}\cdot u_{DRAG}<0 \qquad (46)$$

With regards to the term $f'\left(\overline{x},\dot{\overline{x}}\right)$ in Eq. (45), it is assumed that the magnitude of differential drag is always (or for the most of the maneuver) sufficient to render Eq. (45) negative. This boundary problem in the Lyapunov approach was previously studied in Ref. [13] for the general problem of spacecraft control via on-off thrusters (Eqs. (40) and (44) from [13]), and more specifically in Ref. [12] for the case of differential drag (Eq. (19) and following discussions in [12]). The work here presented makes use of the results presented in Refs. [12,13] to choose reasonable reference dynamics and orbit altitudes for the numerical simulations, such that the available drag forces can counteract the nonlinear terms during the maneuvers.

In addition, an adaptive methodology as the one presented in Ref. [12] may be considered and derived, so that poorly chosen initial reference dynamics can be adjusted during the maneuver to ensure that the condition of Eq. (45) is respected.

The above suggestions for further developments are considered beyond the scope of this work, and may lead to new differential drag based roto-translational adaptive control.

Now, defining

$$v=2\overline{e}_\rho^TPLB \qquad (47)$$

The control signals are obtained as three possible values per thruster. Fig. 6 depicts the resulting three sail scenarios.

$$\overline{u}_i=-sign(v_i)\begin{cases}\sum_{i=1}^8\overline{u}_i>0\to\text{target opens sail (CASE1)} \\ \sum_{i=1}^8\overline{u}_i=0\to\text{target and chaser have closed sail (CASE2)} \\ \sum_{i=1}^8\overline{u}_i<0\to\text{chaser opens sail (CASE 3)}\end{cases} \qquad (48)$$
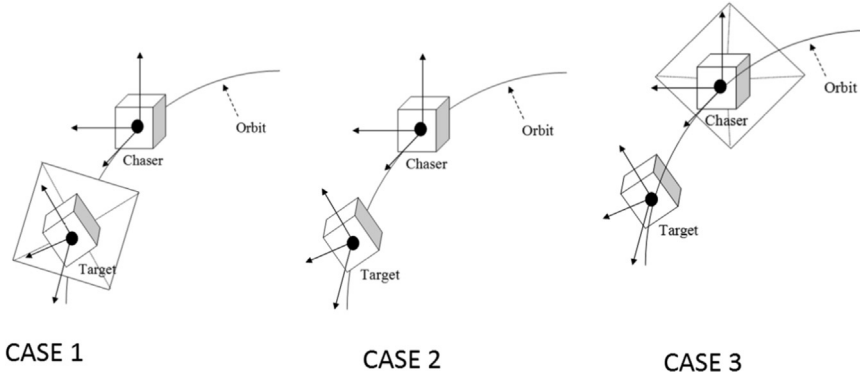
Fig. 6. Target opens its sail (LEFT); Target and chaser have closed sail (CENTER); Chaser opens its sail (RIGHT).

6.4. Lyapunov attitude control strategy

To study the stability of Eq. (38) under virtual thrusters actuation, the Lyapunov approach is used, by selecting as a candidate function:

$$V = e^T P e \qquad (49)$$

With $P = P^T > 0$. Differentiating Eq. (49) along the trajectories in Eq. (38), leads to

$$\dot{V} = \dot{\bar{e}}_\vartheta P e + \bar{e}_\vartheta^T P \dot{\bar{e}}_\vartheta \qquad (50)$$

$$\dot{V} = \bar{e}_\vartheta^T P A \bar{e}_\vartheta + \bar{e}_\vartheta^T A^T P \bar{e}_\vartheta + 2\bar{e}_\vartheta^T P B (H\bar{u} \cdot u_a - \overline{w}) \qquad (51)$$

For a specific symmetric positive definite matrix Q, the matrix P is found as unique solution of the Lyapunov equation:

$$PA + A^T P = -Q \qquad (52)$$

Substituting Eq. (52) in Eq. (51) leads to

$$\dot{V} = -\bar{e}_\vartheta^T Q \bar{e}_\vartheta + 2\bar{e}_\vartheta^T P B (H\bar{u} \cdot u_a - \overline{w}) \qquad (53)$$

Since the first term is always negative definite, in order to be able to prove stability via Lyapunov analysis, the controller needs to be derived to ensure the second terms is at least negative semi-definite.

$$2\bar{e}_\vartheta^T P B (H\bar{u} \cdot u_a - \overline{w}) < 0 \qquad (54)$$

With the same approach and same considerations of the translational case, the control strategy is defined as

$$2\bar{e}_\vartheta^T P B H \bar{u} \cdot u_a < 0 \qquad (55)$$

That means

$$v = 2\bar{e}_\vartheta^T P B H \qquad (56)$$

$$\bar{u}_i = -sign(v_i) \qquad (57)$$

Because the drag force acts only along the negative y direction, this strategy needs to be changed into

$$\bar{u}_i = \frac{v_i - |v_i|}{2v_i} \qquad (58)$$

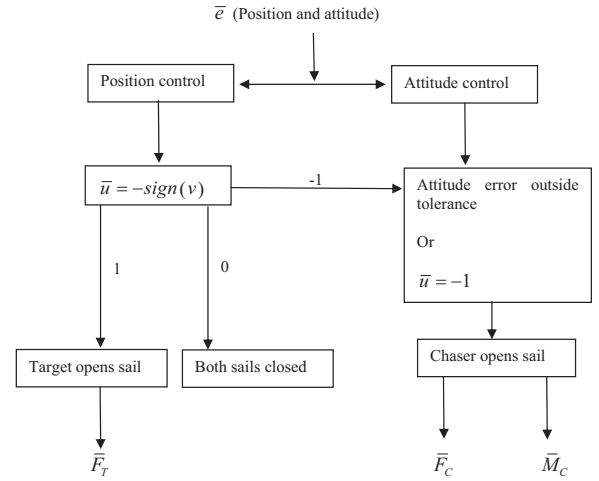When one or more thrusters are active, the control system determines their barycenter. A set of coordinates is

Fig. 7. Full control scheme.

associated to each thruster (see Fig. 5).

$$\begin{cases} \bar{u} = [u_1, u_2 \ldots, u_8] \\ X_g = [X_1, X_2 \ldots, X_8] \\ Z_g = [Z_1, Z_2 \ldots, Z_8] \end{cases} \qquad (59)$$

And the new center of pressure is calculated as the barycenter of the thrusters that are active at any given time, as follows:

$$X_{gg} = \frac{\sum X_i \cdot u_i}{n} \qquad (60)$$

$$Z_{gg} = \frac{\sum Z_i \cdot u_i}{n} \qquad (61)$$

where n is the number of active virtual thrusters, which can range from 1 to 8.

The control system moves the sail to the new center of pressure and a moment around either or both controlled axes can be exerted.

Fig. 7 illustrates the full control strategy. F_T, F_C, and M_C represent drag forces on the target, chaser, and aerodynamic torque on the chaser, respectively. The strategy is divided into two logical loops: the position control loop selects the command $\bar{u}$. The attitude control loop has the

authority to override the position loop, selecting the opening of the chaser's sail if the angular error exceeds the threshold.

7. Numerical simulations

In this section, results of the simulations are shown. First, the behavior of the chosen satellites for the same maneuvers is examined, and then the role of the factors that can influence the system response (i.e., mass, surface area of the sail, and gain parameters) is studied. In order to solve the LQR problem ($K=$LQR(A,B,Q_{LQR},R_{LQR})) as Eq. (26), two parameters are needed to be chosen: the scalar R_{LQR} and the matrix Q_{LQR}.

The simulations were performed in Simulink, using two 6DOF blocks to simulate the dynamics of each spacecraft, taking into account up to J_4 with the Zonal Harmonic Gravity Model, and using the variable density model NRLMSISE-00 Atmosphere Model to compute the drag. The NRLMSISE-00 Atmosphere Model in Simulink was used with default values for local apparent solar time, input flux and magnetic index. The first subsection presents the graphical and numerical results of a Rendezvous maneuver. The following subsection focuses on the rephasing maneuver, considering chaser and target initially placed on the same orbit. The last subsection analyzes the influence of the main parameters that affect the dynamical behavior of the system in a maneuver: the surface area of the sail and the gain R_{LQR}.

7.1. Rendezvous maneuver

Chosen gains for the position control are $R_{LQR}=10^{17}$ and $Q_{LQR}=I_{4\times4}$. The rendezvous maneuver is assumed to be finalized when the distance between the spacecraft is below 10 m. The initial conditions are the same for all the simulations. All the parameters are contained in Table 1. Graphs for CanX-2 are shown in Fig. 8, while Table 6 summarizes the results for the same maneuver executed by the other spacecraft.

The attitude error, the lift forces, and the gravitational perturbations can generate a displacement of the two spacecraft along the z-axis of the *LTRF*. Given its very low entity, it is neglected here.

Table 2 shows the initial relative condition of the two spacecraft in the *LTRF* system and Table 3 the main spacecraft parameters.

The desired state in terms of Euler Angles is the alignment of the *BCRF* with the *LCRF* such that the errors must approach zero, and a tolerance of 15 deg is chosen.

Discrete (step) signals used to command the displacement of the center of pressure are also shown in Fig. 8,

along with discrete (step) signals for target and chaser sails' opening. The number of openings is calculated in order to evaluate the cost of the maneuver for the chosen parameters; in fact, increasing the number of openings implies greater energy consumption and orbital decay (Table 5).

The dynamical behavior chosen for the hypothetical mechanical system representing the sail is based on preliminary data available from the PADDLES sail subsystem currently developed at UFL. When the spacecraft orientation is out of tolerance, a step signal (e.g. Fig. 8) is generated and fed to a first order dynamical system, whose time evolution represents the dynamics of offsetting the center of pressure. In other words, the time response represents the rate at which the surface is moved in the back of the satellite. The step signal lasts a minimum of 1 s and is held until the angular error comes back under the prefixed limits, while the dynamical system has a time constant of 1 s. A similar approach is used for the simulations of the opening or closing of the sail, where the step input (e.g. Fig. 8) is instead not allowed to last less than 5 s. The first order dynamical system associated with it has a slower time response (the time constant is 5 s).

The lower bounds on the step inputs durations impose upper limits on the frequency of actuation. Any command to change the center of pressure with frequency higher than 1 Hz is ignored by the control system, while this limitation is 0.2 Hz for the opening/closing commands.

The details about altitude loss are provided in Table 4 and they can be evaluated in relationship with the number of openings of the target's and chaser's sails, shown in Table 5.

The most important results for the other spacecraft considered here are displayed in Table 6.

OCSD and *EDSN* have the same sail dimensions and surface area, but differing mass. This results in different behavior for attitude stabilization and position control. The *EDSN* needs less time to complete the same maneuver because of the different mass and moments of inertia.

CanX-2 and *OCSD* have comparable masses but different dimensions, affecting the moments of inertia of the system. Since *CPOD* has the highest mass, a bigger surface area enables it to maneuver in only 1.20 days with the fewest numbers of openings.

Atmocube is the lightest spacecraft, with a high ratio between drag sail surface area and its dimensions. This allows it to complete the maneuver in the shortest time, with the smallest orbital decay.

While a general analysis of all parameters affecting the performances may be unlimited, each mission and spacecraft should be analyzed and tuned individually. However,

Table 1
Satellite and orbit parameters.

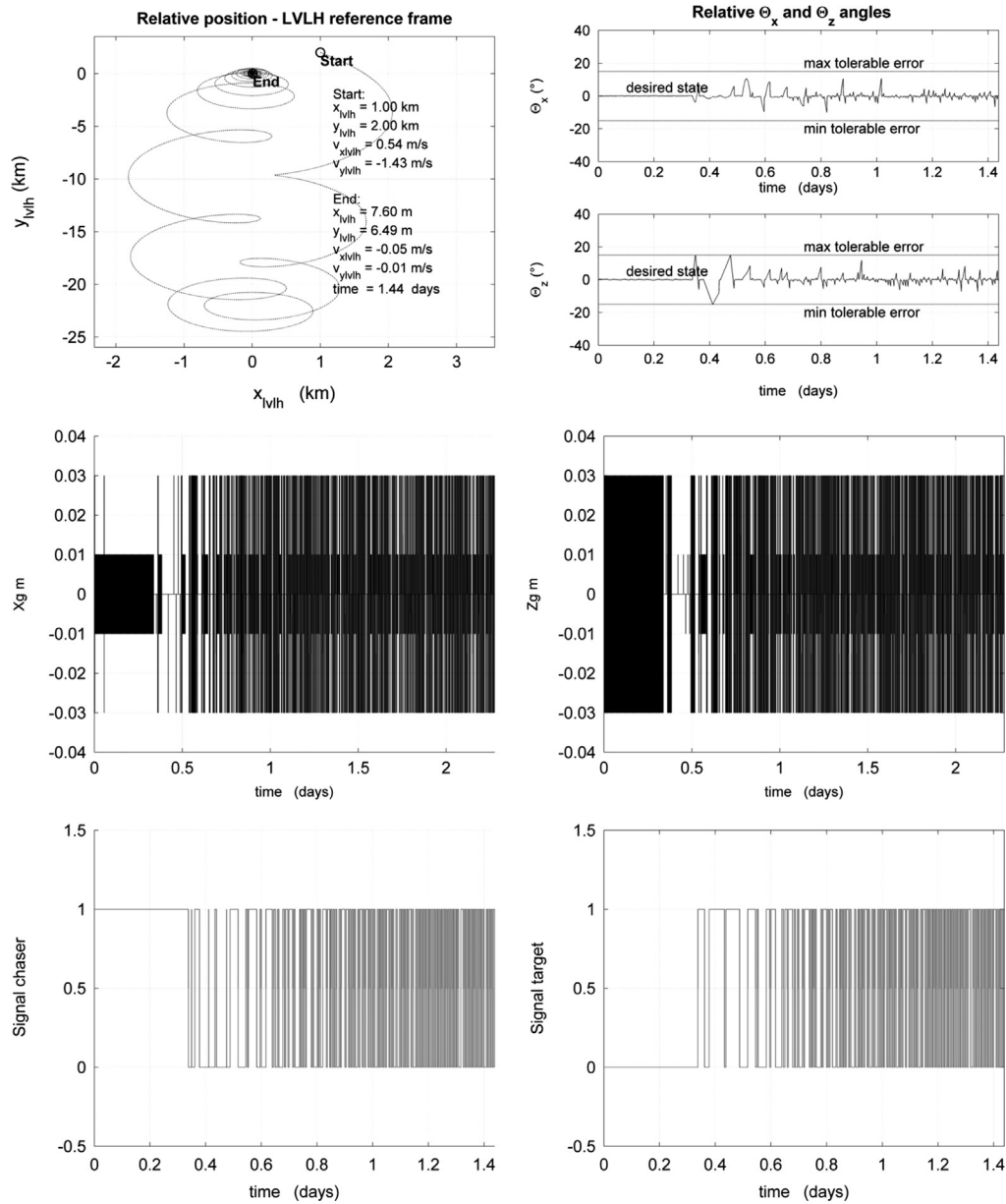|					
C_D		2.6	Orbit inclination	deg	80
μ	km³/s²	398,600	Right ascension	deg	270
J_2		$1.08e-3$	e_{Target}		0
Radius of the Earth	km	6378.14	e_{Chaser}		10^{-4}
Semi-major-axis	km	6778.10	True anomaly target	deg	45
Argumentum of perigee	deg	90	True anomaly chaser	deg	45.017

Fig. 8. CanX-2 x–y trajectory (TOP LEFT); Relative Euler's angles (TOP RIGHT); Center of pressure discrete displacement in X (CENTER LEFT) and Y (CENTER RIGHT) directions; D) CanX-2 Chaser (BOTTOM LEFT) and Target (BOTTOM RIGHT) open/close signals.

Table 2
LVLH-initial and expected final conditions.

Initial condition			Expected final conditions		
Initial x_{LVLH}	km	1.00	Final x_{LVLH}	km	0.00
Initial y_{LVLH}	km	2.00	Final y_{LVLH}	km	0.00
Initial vx_{LVLH}	km/s	5.43e−4	Final vx_{LVLH}	km/s	0.00
Initial vy_{LVLH}	km/s	−1.43e−3	Final vy_{LVLH}	km/s	0.00

Table 3
CanX-2 satellite parameters.

Satellite		CanX-2	Total mass chaser	kg	4.5
Dimension	cm	$8 \times 8 \times 21$	S_{Sail}	m²	1.0
Total mass target	kg	4.5	S_{min}	m²	0.064

the simulations presented herein serve as proof of concept for the proposed control methodology, performing successfully in all chosen cases.

7.2. Rephasing

In the Rephasing maneuver, the target and chaser start in the same orbit but differ in true anomaly. The maneuver consists of changing their relative true anomaly. Table 7

shows the initial conditions of both spacecraft and Table 8 presents the initial and expected condition of the chaser spacecraft in *LTRF*. As done in the previous subsection, CanX-2 plots are presented in Fig. 9 and Table 10 summarizes the results for the other spacecraft.

Some difficulties are observed in the attitude control to keep the Euler angles' errors within the threshold. This may be overcome by tuning new control gains, for example. This simulation is shown to critically demonstrate a

case where the proposed technique encounters its limitations. Many factors come into play (mass, sail surface area, required tolerance on attitude alignment, etc.) and it is expected for some maneuvers to not be feasible. Roughly speaking, some simulations may simply show that the tolerance on attitude alignment cannot be met, given the chosen combination of spacecraft, sail, and control gains.

Table 9 shows the details about the cost of the maneuver in terms of number of openings of the sail and altitude loss for all the analyzed spacecraft.

Table 10 shows the summary for all the simulations performed using the other spacecraft.

7.3. Influence of the parameters: PADDLES satellite

The PADDLES case is now examined. Its characteristics are initially chosen as in Table 11. In this section the influence of two key parameters that can change the behavior of the system is analyzed: the gain R and the surface area of the sail S_{Sail}. The same rendezvous maneuver for all the previous simulations is used (Table 1) and the initial conditions in *LTRF* are shown in Table 2.

For this maneuver, the results show how the surface area of the sail and gain-position can influence the dynamics of the satellites and the maneuvering time.
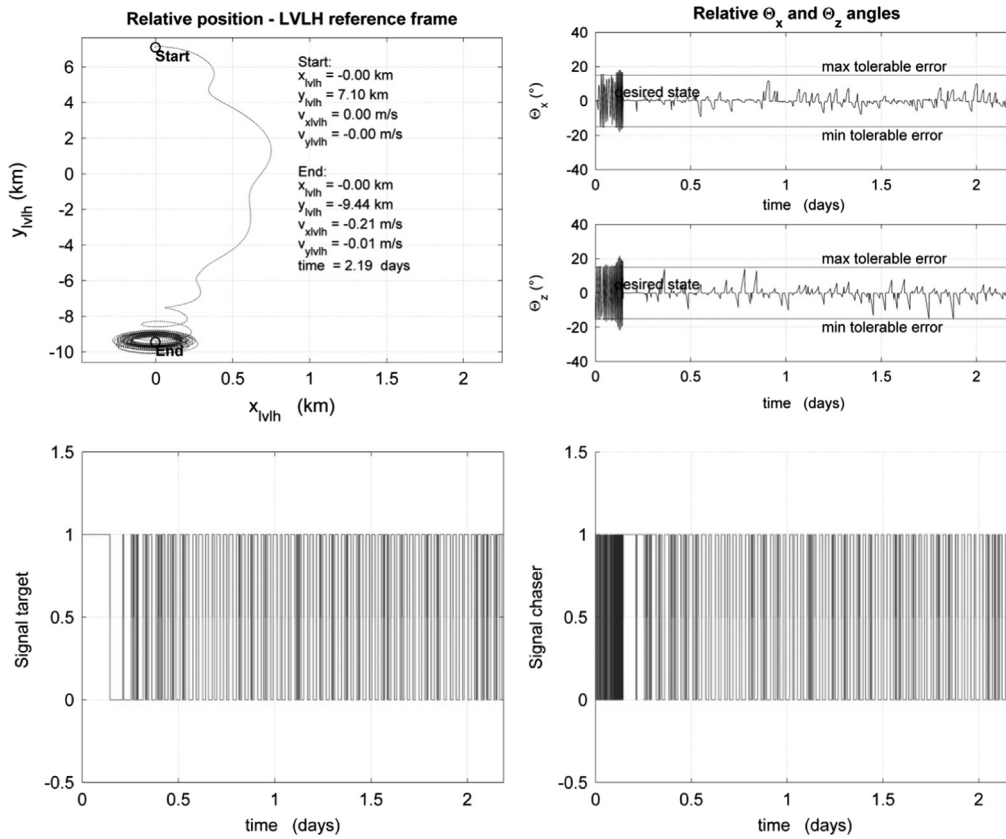
Table 4
CanX-2 altitude parameters.

Initial altitude target	km	410.39
Initial altitude chaser	km	411.39
Loss of altitude target	km	4.93
Loss of altitude chaser	km	5.24
Total maneuvering time	Days	1.44

Table 5
CanX-2 relationship between number of openings and loss of altitude.

	Chaser	**Target**
Number of openings	89	86
Loss of altitude %	1.23	1.16
Loss of altitude km	5.24	4.93

Table 6
Rendezvous numerical simulations comparison.

Satellite name		**CanX-2**	**OCSD**	**EDSN**	**CPOD**	**Atmocube**
Mass	kg	4.5	4	2.5	6	1.5
Surface sail	m^2	1	1	1	1.5	0.5
Dimensions	cm	$8 \times 8 \times 21$	$10 \times 10 \times 16$	$10 \times 10 \times 16$	$10 \times 10 \times 33$	$10 \times 10 \times 10$
Gain position R		10^{17}	10^{17}	10^{17}	10^{17}	10^{17}
maneuvering time	days	1.44	1.56	0.92	1.20	0.40
No. openings chaser		89	105	120	74	109
Loss of altitude chaser	%	1.23	1.56	1.43	1.07	0.69
Loss of altitude chaser	km	5.24	6.64	6.11	4.57	2.94

Table 7
Satellite and orbit parameters.

C_D		2.6	Orbit inclination	deg	80
μ	km^3/s^2	398,600	Right ascension	deg	270
r_{earth}	km	6378.14	e_{Target}		10^{-4}
J_2		$1.08e-3$	e_{Chaser}		10^{-4}
Radius of the Earth	km	6378.14	True anomaly$_{target}$	deg	20
Semi-major-axis	km	6778.10	True anomaly$_{Chaser}$	deg	20.06
Argumentum of perigee	deg	90			

Table 8
LVLH-initial and expected final conditions.

Initial condition				Expected final conditions		
Initial x_{LVLH}	km	$-3.47e-003$		Final x_{LVLH}	km	$-6.61e-003$
Initial y_{LVLH}	km	$7.09e+000$		Final y_{LVLH}	km	$-9.46e+000$
Initial vx_{LVLH}	km/s	$7.55e-007$		Final vx_{LVLH}	km/s	$-1.07e-006$
Initial vy_{LVLH}	km/s	$-2.75e-007$		Final vy_{LVLH}	km/s	0.00

Fig. 9. CanX-2 *x–y* trajectory (TOP LEFT); Relative Euler angles (TOP RIGHT); open/close signal target (BOTTOM LEFT) and Chaser (BOTTOM RIGHT).

Table 9
CanX-2 number of openings and loss of altitude.

		Chaser	Target
Number of openings		128	88
Loss of altitude	%	1.53	1.47
Loss of altitude	km	6.77	6.51

Table 11
PADDLES satellite parameters.

Satellite		**PADDLES**	Total mass chaser	kg	3
Dimension	cm	$10 \times 10 \times 30$	S_{Sail}	m^2	0.5
Total mass target	kg	3	S_{min}	m^2	0.01

Table 10
Summary table.

Satellite name		CanX-2	*OCSD*	*EDSN*	*CPOD*	Atmocube
Mass	kg	4.5	4	2.5	6	1.5
Surface sail	m^2	1	1	1	1.5	0.5
Dimensions	cm	$8 \times 8 \times 21$	$10 \times 10 \times 16$	$10 \times 10 \times 16$	$10 \times 10 \times 33$	$10 \times 10 \times 10$
Gain position		10^{17}	10^{17}	10^{17}	10^{17}	10^{17}
Maneuvering time	hs	52.51	52.46	35.49	10.71	32.39
Maneuvering time	days	2.19	2.19	1.48	0.45	1.35
No. openings chaser		128	206	216	54	242
Loss of altitude chaser	%	1.53	1.76	1.95	0.12	1.45
Loss of altitude chaser	km	6.77	7.78	8.61	0.55	6.42

Fig. 10 shows the dynamical behavior in the *x-y* plane of the spacecraft for different surface areas of the sail; a greater area generally leads to a smaller maneuver time and to better stabilize the attitude of the chaser spacecraft (see Fig. 11).

Table 12 shows that setting the gain parameter $R = 10^{17}$ for the PADDLES satellite results in the best configuration

when $S_{sail} = 1$ m^2. However, there is no linear relationship between sail's area and time of convergence.

Increasing the area of the sail doesn't always lead to smaller times of convergence. In fact, the drag influences the relative dynamics of both spacecraft, not only the behavior of one.

While a very low drag force would be detrimental to retain control authority, too high of a force would work against reaching the established rendezvous condition (below 10 m); creating a limiting cycle response issue. In such cases other parameters would need recalibration, as, for example the maximum frequency of actuation.

Fig. 12 shows the gain R's influence on the time of convergence of the maneuver. Increasing the position gain R from 10^{16} to $5 \cdot 10^{17}$, doubles the maneuvering time. This is a negative impact, which is compensated by better stabilization of the orientation of the chaser, as shown in Fig. 13. A higher gain R leads to a larger number of openings of the chaser's sail, thus increasing the attitude control time and reducing the Euler angles' error.

In Table 13 the influence of the gain parameter is summarized.

8. Conclusion

The literature of the past three decades focused on the idea of spacecraft drag-based propellant-less translational maneuvers. The present work demonstrates that the roto-translational dynamics can be controlled, provided that a spacecraft can control its drag magnitude and point of application. The idea of a deployable and retractable drag sail, capable of offsetting its center of pressure, appears as a viable solution for generation of orbital control forces and ram-alignment control torques. The proposed approach translates these forces and torques into eight virtual thrusters in the back-end of a spacecraft, thus enabling the use of classical Lyapunov-based control, and subsequent mapping of the on-off virtual thrusters commands into open-close commands and center of pressure offset commands to the sail.

The virtual thrusters approach priorities attitude control over position control, since attitude dynamics responses are much faster. This choice is supported by numerical simulations, were the position accuracy in executing rendezvous and rephasing maneuvers remains unaltered, while the attitude control can be largely affected by changing the spacecraft sail

Table 12
Relationship among control gain, sail surface area, length of maneuver, and number of sail openings.

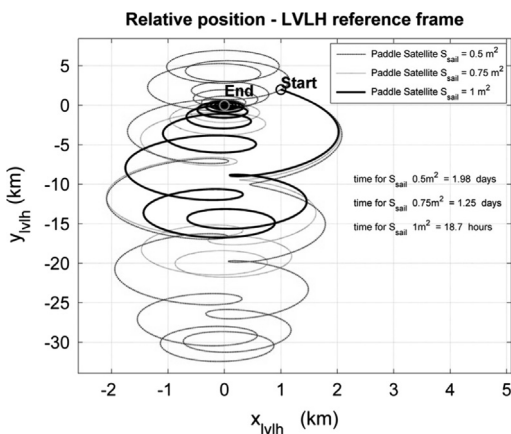| R		10^{17}	10^{17}	10^{17}
S_{sail}	m^2	0.5	0.75	1
Maneuvering time	days	1.98	1.25	0.78
No. openings chaser		106	71	36

Fig. 10. x–y Trajectory for different Sail's areas.
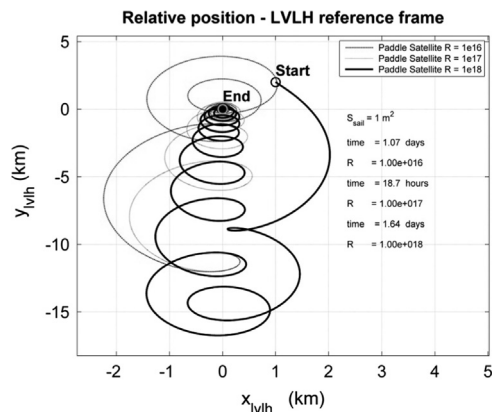

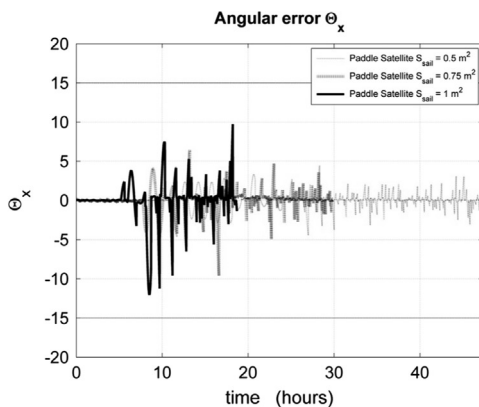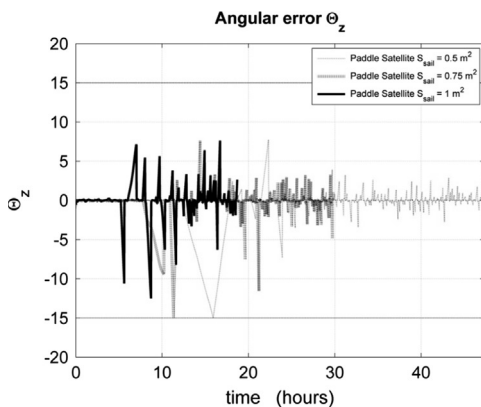**Fig. 12.** x–y Trajectory for different gain-positions with $S_{sail} = 1$ m^2.

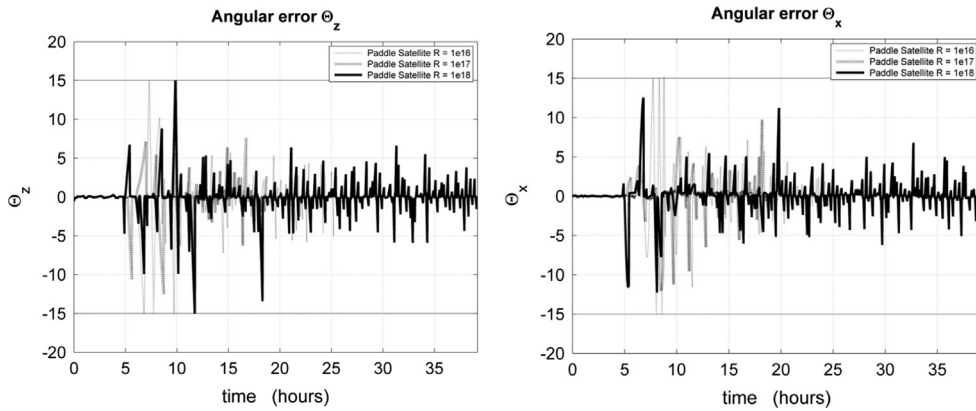**Fig. 11.** Angular errors for different Sail's areas.

Fig. 13. Angular errors for different gain-positions with $S_{sail} = 1$ m^2.

Table 13
Relationship among control gain, sail surface area, length of maneuver, and number of sail openings.

R		10^{16}	10^{17}	10^{18}
S_{sail}	m^2	1	1	1
Maneuvering time	days	1.06	0.78	1.64
No. openings chaser		75	36	140

surface area and the control gains. Numerical simulations need to be performed to correctly tune the controller gains to obtain satisfactory attitude control every time a new ratio between surface area of the sail and mass of the spacecraft is introduced.

Six existing or planned nanosatellite missions are used to validate the methodology by simulating rendezvous and rephasing maneuvers and implementing the dynamics of a realistic mechanism for the drag sail operations.

The numerical simulations show that the proposed approach is an effective method for all the suggested maneuvers and analyzed spacecraft. This novel strategy particularly controls the chaser's orientation for all the maneuvers, enabling the continuous use of differential drag forces for relative maneuvering.

Future work is suggested towards the derivation of an adaptive version of the Lyapunov-based controller, so that unrealistic initial linear reference dynamics can be adjusted during the maneuver.

References

[1] D. Rankin, D.D. Kekez, R.E. Zee, F.M. Pranajaya, D.G. Foisy, A., M. Beattie, The CanX-2 nanosatellite: expanding the science abilities of nanosatellites July–October, Acta Astronaut. 57 (2–8) (2005) 167–174.

[2] Janson, S.W., Welle, R.P., The NASA optical communication and sensor demonstration program, in: 27th Annual AIAA/USU Conference on Small Satellites, Paper SSC13-II-1, 2013.

[3] Cockrell, J., Alena, R., Mayer, D., Sanchez, H., Luzod, T., Yost, B., Edison Demonstration of SmallSat Networks, in: Small Satellite Conference, Utah State University, paper SSC12-I-5, 2012.

[4] Tyvak Nano-Satellite Systems, LLC of Irvine, California Cubesat Proximity Operations Demonstration (CPOD), 〈http://www.nasa.gov/directorates/spacetech/small_spacecraft/cpod_project.html. UoOaMeJELad〉, 2013 [retrieved 12 November 2013].

[5] Gregorio, A., Bernardi, T., Carrato, S., Kostadinov, L., Messerotti, M., Stalio, R., AtmoCube: observation of the Earth atmosphere from the space to study space weather effects, in: Proceedings of Recent Advances in Space Technologies, Emerging Applications and Opportunities for All; RAST 2003. pp. 188-193. Paper IEEE cat. no. 03EX743.

[6] Lamberto Dell'Elce, Gaëtan Kerschen, Comparison between analytical and optimal control techniques in the differential drag based Rendez-vous, in: Proceedings of the Fifth International Conference on Spacecraft Formation Flying Missions & Technologies, Munich, May 2013. 〈http://www.sffmt2013.org/PPAbstract/4039p.pdf〉, 2013 [retrieved 12 November 2013].

[7] Skyler M. Shuford, Feasibility of CubeSat Formation Flight Using Rotation to Achieve Differential Drag June 2013, Aerospace Engineering, California Polytechnic State University, San Luis Obispo, 2013 retrieved 12 November.

[8] B. Kumar, A. Ng, K. Yoshihara, A. De Ruiter, Differential drag as a means of spacecraft formation control April, IEEE Trans. Aerosp. Electron. Syst.0018-925147 (2) (2011) 1125–1135, http://dx.doi.org/10.1109/TAES.2011.5751247.

[9] Palmerini, G.B., Sgubini, S., Taini, G., Spacecraft Orbit Control using Air Drag, 56th International Astronautical Congress of the International Astronautical Federation, the International Academy of Astronautics, and the International Institute of Space Law, IAC-05-C1.6.10, 2005. doi:10.2514/6.IAC-05-C1.6.10.

[10] R. Bevilacqua, M. Romano, Rendezvous maneuvers of multiple spacecraft using differential drag under J2 Perturbation, J. Guid. Control Dynam. 31 (6) (2008) 1595–1607, http://dx.doi.org/10.2514/1.36362.

[11] Pérez, D., Bevilacqua, R., Lyapunov-based spacecraft rendezvous maneuvers using differential drag, in: AIAA Guidance, Navigation, and Control Conference, Portland, Oregon, 08–11 August, 2011, . http://dx.doi.org/10.2514/6.2011-6630.

[12] D. Pérez, R. Bevilacqua, Differential drag spacecraft rendezvous using an adaptive Lyapunov control strategy, Acta Astronaut. 83 (2013) 196–207, http://dx.doi.org/10.1016/j.actaastro.2012.09.005.

[13] F. Curti, M. Romano, R. Bevilacqua, Lyapunov-based thrusters' selection for spacecraft control: analysis and experimentation, J. Guid. Control Dynam. 33 (4) (2010) 1143–1160, http://dx.doi.org/10.2514/1.47296.

[14] D.A. Vallado, D. Finkleman, A critical assessment of satellite drag and atmospheric density modeling Available online 25 October, Acta Astronaut.0094-5765(2013), http://dx.doi.org/10.1016/j.actaas-tro.2013.10.005. in press.

[15] H.D. Curtis, Orbital Mechanics for Engineering Students Elsevier Aerospace Engineering Series, second ed. Butterworth-Heinemann, 2009, pp. 392–394 and 573–644.

[16] B. Wie, Space Vehicle Dynamics and Control AIAA Education Series, second ed. AIAA, 2008, 307–322, http://dx.doi.org/10.2514/4.860119 eISBN: 978-1-60086-011-9, print ISBN: 978-1-56347-953-3.

[17] Sedwick, R., Schweighart, S.A., Development and analysis of a high fidelity linearized j2 model for satellite formation flying, in: AIAA Space Conference and Exposition, 2001 http://dx.doi.org/10.2514/6.2001-4744.

Mirko Pastorelli obtained his Master's degree (Laurea) in Mechanical Engineering at Politecnico di Torino, Italy in 2013. He spent 6 months at The Advanced Autonomous Multiple Spacecraft Laboratory, directed by Dr. Bevilacqua, as Visiting Graduate Student, working on the research presented in this paper.

Dr. Riccardo Bevilacqua is an Associate Professor of the Mechanical and Aerospace Engineering Department at the University of Florida (UFL). He holds a M.Sc. in Aerospace Engineering (2002), and a Ph.D. in Applied Mathematics (2007), both earned at the University of Rome, "Sapienza", Italy. He was a US National Research Council Post-Doctoral Fellow from 2007 to 2010 and an Assistant Professor at Rensselaer Polytechnic Institute from 2010 to 2014, before joining UFL. He also worked as project engineer in Mission Analysis at Grupo Mecanica del Vuelo, in Madrid, Spain, during 2003. Dr. Bevilacqua's research interests focus on Guidance, Navigation, and Control of multiple spacecraft systems and multiple robot systems.

Stefano P. Pastorelli received the M.S. degree in mechanical engineering and the Ph.D. degree in applied mechanics from Politecnico di Torino, Turin, Italy, in 1992 and 1996, respectively. From 1995 to 1997 he was a Consultant Engineer for a high-tech aeronautical company. He is currently an Associate Professor of Applied Mechanics and Robotics with the Department of Mechanical and Aerospace Engineering at the Politecnico di Torino, Italy. His research interests include functional design of mechanical systems, mechanical power transmission and actuation servosystems, kinematics and dynamics of robots, 3-D motion capture techniques and identification, active human modelling for biomechanics.